

Modulation of storm-time mid-latitude ionosphere by magnetosphere-ionosphere coupling 2

Sebastijan Mrak¹, Joshua Semeter¹, Yukitoshi Nishimura¹, J C Foster², Marc Hairston³, and W A Bristow⁴

¹Boston University

²Massachusetts Institute of Technology

³UT Dallas

⁴University of Alaska Fairbanks

November 21, 2022

Abstract

We describe mid-latitude plasma density striations (MDS) modulating the evening side of Storm Enhanced Density (SED) by magnetosphere-ionosphere coupling. The MDS are magnetically conjugate, and they consist of elongated density structures [enhancements (plumes) and depletions (troughs)] that extend from the equator to the main trough equatorward boundary. Each density perturbation is associated with a flow channel, and they develop progressively at all latitudes. We present a detailed analysis of the MDS during the 7-8 September 2017 storm, by virtue of remote and in-situ observations of the magnetosphere-ionosphere system. We find that the density plumes are a result of local plasma uplift, and poleward and westward plasma transport guided by the adjacent flow channels. While the MDS's troughs bear some resemblance to the depletion patterns associated with equatorial plasma bubbles, it has been found to be quite distinct, both in terms of its observational manifestations and its formation mechanism. Namely, the trough is associated with enhanced flow channels peaking at the edges, with elevated electron and ion temperatures. Crucial spacecraft measurements of plasma parameters in the ionosphere and plasmasphere near the equatorial plane ($L \approx 1.9$) unambiguously show conjugate nature of the MDS. In particular, the magnetospheric electric field intensifications lie just earthward of the injected < 200 keV ions at the ion pressure gradient.

Modulation of storm-time mid-latitude ionosphere by magnetosphere-ionosphere coupling

Sebastijan Mrak¹, Joshua Semeter¹, Yukitoshi Nishimura¹, J. C. Foster², Marc R. Hairston³, W. A. Bristow⁴

¹Department of Electrical and Computer Engineering and Center for Space Physics, Boston University, Boston, MA, USA

²Haystack Observatory, Massachusetts Institute of Technology, Westford, MA, USA

³Center for Space Sciences, University of Texas at Dallas, Richardson, TX, USA

⁴Geophysical Institute, University of Alaska Fairbanks, Fairbanks, Alaska, USA

Key Points:

- We characterize mid-latitude plasma density striations (MDS) using ground-based and in-situ observations.
- The MDS are magnetically conjugate within $L \leq 2.3$, with distinctive flow channels, and elevated plasma temperature.
- We find that one of the electric field excursions along the MDS resided within the ring current pressure gradient.

Corresponding author: Sebastijan Mrak, smrak@bu.edu

Abstract

We describe mid-latitude plasma density striations (MDS) modulating the evening side of Storm Enhanced Density (SED) by magnetosphere-ionosphere coupling. The MDS are magnetically conjugate, and they consist of elongated density structures [enhancements (plumes) and depletions (troughs)] that extend from the equator to the main trough equatorward boundary. Each density perturbation is associated with a flow channel, and they develop progressively at all latitudes. We present a detailed analysis of the MDS during the 7-8 September 2017 storm, by virtue of remote and in-situ observations of the magnetosphere-ionosphere system. We find that the density plumes are a result of local plasma uplift, and poleward and westward plasma transport guided by the adjacent flow channels. While the MDS's troughs bear some resemblance to the depletion patterns associated with equatorial plasma bubbles, it has been found to be quite distinct, both in terms of its observational manifestations and its formation mechanism. Namely, the trough is associated with enhanced flow channels peaking at the edges, with elevated electron and ion temperatures. Crucial spacecraft measurements of plasma parameters in the ionosphere and plasmasphere near the equatorial plane ($L \approx 1.9$) unambiguously show conjugate nature of the MDS. In particular, the magnetospheric electric field intensifications lie just earthward of the injected <200 keV ions at the ion pressure gradient.

Plain Language Summary

Geomagnetic storms are characterized by enhanced ring current, which is an electrical generator that drives enhanced sub-auroral flow in the ionosphere. A prominent consequence is an ionospheric density trough at mid-latitudes in the dusk local time sector. The location of this mid-latitude trough depends on the strength and location of the ring current injections. The trough is an important space weather threat as it facilitates plasma turbulence and it creates steep density gradients. We analyze the electrodynamic of an event, where there were multiple troughs and plasma adjacent enhancements. These mid-latitude density striations were associated with fluctuations in the electric field and convection. We show that the modulation of the electric field is field-aligned, and located earthward of the ring current. We argue the source of the modulation is a competition between electrodynamic carried by subsequent substorm injections, and impulsive enhancement of penetration electric field impacting the low-latitude ionosphere.

1 Introduction

Structured plasma depletions at mid-latitudes have been observed during geomagnetic storms (Greenspan et al., 1991; J. C. Foster & Rich, 1998; C.-s. Huang et al., 2007; Aa et al., 2019; Ma & Maruyama, 2006; Martinis et al., 2015; Zakharenkova & Cherniak, 2020) and attributed to the extreme expansion of equatorial plasma bubbles (EPB). Benchmarks for such an event were set by ground-based observations of the EPB's spatiotemporal evolution (i.e. Ma & Maruyama, 2006; Martinis et al., 2015), showing poleward expansion with a characteristic breakup at the poleward edges. The earlier in-situ observations of deep and highly structured depletions, however, were lacking spatiotemporal context (e.g. Greenspan et al., 1991; J. C. Foster & Rich, 1998; C.-s. Huang et al., 2007). Nevertheless, all events were attributed to EPBs, based on the character of in-situ plasma density depletion with embedded irregularities. The geolocation and timing were discussed in association with sunset conductivity gradients, and the vicinity of the South Atlantic Anomaly (SAA). It was Lin et al. (2007) who has sketched the geomagnetic and local time dependence. Furthermore, they found that the density depletions are paired with eastward-adjacent density enhancement. They termed these features magnetic anomaly density structures (MADS).

We build upon recent observations of mid-latitude density perturbations, during the 7-8 September 2017 geomagnetic storm (Aa et al., 2019; Zakharenkova & Cherniak, 2020). We put the observations in a context of historical literature – specifically, we bolster the conclusions of Lin et al. (2007), expand their analysis through the use of 2D total electron content (TEC) maps and conjugate in-situ observations in the ionosphere and magnetosphere. It is important to emphasize that historical observations were made during “superstorms”, whereas the presented storm was associated with a maximum ring current excursion (SYM/H index) of ~ 150 nT, and at solar minimum. Nevertheless, the storm caused a sequence of episodic space weather effects, ranging from strong Ground Induced Currents in Scandinavia (Dimmock et al., 2019; Piersanti et al., 2019), Global Navigation Satellite Systems (GNSS) disruptions (Berdermann et al., 2018), extreme plasmasphere erosion (Obana et al., 2019), and a plethora of ionospheric phenomena (Aa et al., 2018, 2019).

A typical picture of the storm-time mid-latitude ionosphere at dusk consists of enhanced plasma density transported from lower latitudes (the Storm Enhanced Density - SED) (J. C. Foster, 1993), which is swept sunward by the Sub-Auroral Polarization Stream (SAPS) (J. C. Foster & Vo, 2002; J. C. Foster et al., 2007). The process of plasma redistribution is magnetically conjugate (J. C. Foster & Coster, 2007), predominantly driven by the penetration electric field (Kelley et al., 1979; J. C. Foster & Rich, 1998), and leaves a void in night-time equatorial region (Immel et al., 2005). The mid-latitude trough on the poleward boundary of the SED is a consequence of enhanced recombination (Schunk et al., 1976) driven by magnetosphere-ionosphere coupling processes (P. C. Anderson et al., 1991, 1993; Goldstein et al., 2005; E. Mishin et al., 2017).

The present study builds upon this picture by showing additional features in the (predominantly) mid-latitude ionosphere produced by a series of impulsive electrodynamic events. Specifically, we present detailed observations of SED segmentation on the evening side by enhanced plasma flows. The segmentation is morphologically similar to the plasma density striations observed by Lin et al. (2007). However, our analysis shows that the resulting density perturbations extend up to the mid-latitude trough at the poleward end. Hence, we termed the density striations as mid-latitude density striations (MDS), as the density perturbation is the most pronounced consequence. The detailed TEC maps were augmented by several fortuitous spacecraft flybys in the ionosphere and magnetosphere. The magnetospheric measurements show that one of the episodic electric field excursions, seen as a meridional flow channel in the ionosphere, resided within the ring current ion pressure gradient, just earthward of the injected <200 keV ions.

2 Observations

Solar wind parameters and geomagnetic indices for the 7-8 September 2017 geomagnetic storm are shown in Figure 1. The first three panels show Interplanetary Magnetic Field (IMF) components, solar wind speed and pressure, and geomagnetic indices for a period of ± 36 hours around the storm onset. The storm commencement coincided with an arrival of an interplanetary shock (event (0)) preceding the arrival of a coronal mass ejection with increased solar wind speed ~ 700 km/s. The solar wind data was taken from the OmniWeb database. The shock arrived at 23:10 Universal Time (UT) on September 7, while abruptly increased negative B_Z (< -30 nT) at 23:20 UT marks the start of the sharpest drop in SYM/H, that is the beginning of the storm main phase (event (1)). The ring current development was extremely rapid, as SYM/H decreased from -20 to -100 nT in about 10 minutes. SYM/H reached -150 nT about an hour later. Meanwhile, two episodic auroral electrojet intensifications with a strength of $AL \sim 2000$ nT (AL, shown in Figure 1f), events (2) and (3): first at 23:45 UT, and the second at 00:20 UT on September 8th. K_p index reached the value of 8 during the storm main phase. The storm (ring current) recovery began at $\sim 01:10$ UT.

117 **2.1 Ground-based: Ionosphere**

118 **2.1.1 Storm-time TEC evolution**

119 We begin the analysis at around 22:00 UT on September 7, about an hour before
 120 the shock's arrival. We focus on the spatial development of ionospheric TEC over the
 121 American longitude sector and its relationship with high latitude convection. We uti-
 122 lized the Super Dual Auroral Radar Network (SuperDARN) from North America to com-
 123 pile high-resolution, local divergence-free maps of F-region $\mathbf{E} \times \mathbf{B}$ convection (Bristow et
 124 al., 2016). Figure 2 shows the spatiotemporal development of the high latitude convec-
 125 tion (top panels), and Global Positioning System (GPS) derived TEC maps at 1 hour
 126 cadence. Vertical TEC maps are obtained from the MIT Haystack automatic procedure
 127 (Rideout & Coster, 2006; Vierinen et al., 2016). Blue vectors in the SuperDARN con-
 128 vection mark actual back-scatter, whereas grey vectors are the divergence-free estimates.

129 After two hours of negative IMF B_Z , Figures 2a-b show a coherent sunward plasma
 130 flow channel between 60-70 MLAT, guiding high density plasma from mid-latitudes to-
 131 wards the cusp and into the polar cap. An hour later in Figure 2c, the flow channel ex-
 132 panded equatorward by ~ 10 degrees, now with highly structured flow vectors. On the
 133 dusk side of the enhanced sunward flow channel, the mid-latitude trough $T0$ was devel-
 134 oping. A distinct breakup $B1$ in the enhanced sunward flow developed at 18:00 MLT.
 135 Large TEC striations appear just equatorward of that flow breakup, located in the east-
 136 ward (evening side) SED boundary, and are hereafter referred to as the mid-latitude den-
 137 sity striations (MDS). The MDS in Figure 2c consists of two troughs, denoted as $T1$ and
 138 $T2$ (outlined with broken lines), and two density plumes $P1$ and $P2$, eastward adjacent
 139 to the troughs. All parts of the MDS extended meridionally toward the equator and were
 140 magnetically conjugate. However, the observations did not capture their total extent due
 141 to sparse sampling over the Atlantic.

142 Figure 2d shows the MDS at 1:00 UT. The $T1$ trough developed significantly in
 143 density and width, reaching a depletion level similar to the main mid-latitude trough and
 144 a highly uniform width of ~ 300 km (width similar to the adjacent plume $P1$). Simul-
 145 taneously, the westward adjacent plume $P1$ also increased in density, reaching the peak
 146 TEC near 40° MLAT of 30 TECu (1 TECu = 10^{16} electrons per square meter), in con-
 147 trast to the trough of 3 TECu just 300 km east. The $P1 - T1$ pair was magnetically
 148 conjugate as described in detail by Aa et al. (2019). The $T1$ trough did cut across the
 149 Equatorial Ionization Anomaly (EIA), whereas the $P1$ plume appears to be a highly elon-
 150 gated poleward extension of the EIA with a similar TEC at ~ 1 UT. At that point, the
 151 auroral oval expanded beyond the SuperDARN coverage (~ 55 MLAT), hence from this
 152 point onward all the back-scatter came from the auroral region.

153 Another density plume $P2$, eastward adjacent to the trough $T1$ is noteworthy. The
 154 $P2$ plume was spatially spread in contrast to the very narrow plume $P1$. While a plume-
 155 trough ($P1-T1$) pair much resembles the Lin et al. (2007) illustration of MDS spatial po-
 156 sition, the additional density plume ($P2$) eastward adjacent to the $T1$ is a new feature
 157 that was not reported by Lin et al. (2007), as it doesn't extend to lower latitudes. Rather
 158 it did extend westward between the two parallel troughs, likely due to the presence of
 159 the SAPS flow.

160 At about 2:00 UT, the MDS began to collapse, when the parallel troughs $T0$ and
 161 $T1$ converged near 18 MLT, 45 MLAT in Figure 2e. The most pronounced change in the
 162 MDS appearance was a structural deformation in the secondary trough $T1$. The secondary
 163 trough dissolved from a compact elongated density structure into density holes highlighted
 164 in the TEC maps by the white circles. Simultaneously, the westward adjacent plume $P1$
 165 disappeared, and the MDS slowly decayed away as illustrated in panels Figure 2f-h.

166

2.1.2 The development of MDS

167

168

169

170

171

172

173

174

175

176

177

178

179

180

The development of the MDS is analyzed in greater detail following Figure 3. We evaluate connections between the MDS, high latitude convection, and the sunset terminator. We utilize differential TEC (ΔTEC) maps to investigate the spatiotemporal development of the density structures, independent of the background value. The ΔTEC maps were obtained by taking a difference between two consecutive TEC maps at a 5-minute resolution, $\Delta\text{TEC}_t = \text{TEC}_t - \text{TEC}_{t-5\text{min}}$. We use the differential TEC maps as a qualitative indicator of temporal increase/decrease (red/blue) in regional column plasma density. The polarization terminator (PT) J. Foster and Erickson (2013) consists of points at a given altitude (here 100 km) where the sunset terminator at either end of the magnetic field line through that point. The PT and sunset terminators at two altitudes (100 km and 300 km) are depicted in Figure 3a – middle panel. The top panels in Figure 3 consists of the SuperDARN maps overlaid on top of the TEC maps. The TEC and subsequent differential TEC maps (middle and bottom panels) have overlaid position of the PT.

181

182

183

184

185

186

187

188

189

190

191

192

193

At 23:00 UT, Figure 3a, the ΔTEC map shows a large region of increasing density at mid-latitudes (i.e., the SED, red), due to local plasma uplift, and transport from lower latitudes (blue) (J. C. Foster, 1993). A local, longitudinally elongated TEC decrease just poleward of the SED is clearly identified in the differential TEC map, despite this region was still in the sunlit ionosphere. This region of local TEC decrease is co-located with enhanced sunward plasma flow identified by the SuperDARN convection map. We refer to the longitudinally decreased TEC region as the mid-latitude trough. We define the border between the mid-latitude trough and the SED the trough equatorward boundary (TEB). Ten minutes later, (Figure 3b, at the time of the shock arrival (event (0))), the ΔTEC map indicates an equatorward expansion of the mid-latitude trough and marks the first appearance of the $T1$ and $T2$ troughs. At 23:30 UT, Figure 3d, ΔTEC maps, and the SuperDARN convection clearly show co-location of the breakup point $B1$, with the poleward edge of the MDS just west of 18:00 MLT.

194

195

196

197

198

199

200

201

An equatorward deflection of the otherwise sunward flow co-located with adjacent MDS lasted for more than half an hour, the time period of episodic density increase in the MDS. The ΔTEC map indicate that the MDS emerged as slightly westward-tilted meridional structures, but already present at all latitudes below 55 MLAT at 23:30 UT. The ΔTEC maps reveal the presence of the MDS before they became apparent in the TEC maps at about 23:50 UT. Interestingly the MDS cross the PT near 40 MLAT. At the 00:10 UT Figure 3h), the peak-to-trough ($P1-T1$) amplitude of the MDS significantly increased, reaching values of 30 – 3 TECU , respectively.

202

203

204

205

206

207

208

209

The SuperDARN backscatter-estimated flow speed before and during the MDS development (22:00 – 01:00 UT) has constantly exceeded 1000 m/s as depicted in Figure 4. The Figure depicts equatorward expansion of the flow channel in excess of 10°MLAT , as well as it shows zonally and meridionally averages flow speeds. The backscatter came from the region of increased plasma density withing the SED plume, and the region of depleted density just poleward of it. The backscatter locations with respect to the TEC structures are depicted in the top panels of Figure 3, and in the supplemental movie S1 with 2 minute resolution.

210

2.1.3 The equatorial electrojet

211

212

213

214

215

216

We estimate the strength of the equatorial electrojet, and consequently the strength of the penetration electric field (PEF) utilizing low latitude magnetometers. We use data from Huancayo (HUA, Peru. 1.17°MLAT) and Kourou (KOU, French Guyana. 8.62°MLAT), to estimate the strength of the equatorial electrojet, and $\mathbf{E} \times \mathbf{B}$ upward drift at the equator (D. Anderson, 2002; Kikuchi et al., 2010). The estimated strength of the electrojet-imposed magnetic field deflection is shown in Figure 5. The magnetogram indicates the

217 presence of a long-lasting enhanced equatorial electrojet (positive ΔH deflection), which
 218 indicates a long-lasting presence of the eastward electric field. According to statistical
 219 formulae (cf. D. Anderson, 2002), $\Delta H \sim 100$ nT corresponds roughly to plasma uplift
 220 at equator $v_{up} \sim 40$ m/s. Four events identified by geophysical drivers are marked on the
 221 magnetogram. Two outstanding intensifications are aligned to the storm onset, labeled
 222 (1), and the second substorm injection labeled (3).

223 The MDS began to develop right after the storm onset (1), at the time of abruptly
 224 enhanced electrojet. The striations, however, steadily increased in amplitude in the next
 225 hour, despite a decrease in the electrojet. By the time of the next electrojet intensifica-
 226 tion at $\sim 00:30$ UT (3), the MDS were already well developed. An eastward electric field
 227 was present at the American longitude sector until ~ 4 UT, which is local midnight in
 228 Huancayo. The inferred eastward electric field was likely the driver of upward and pole-
 229 ward plasma transport resulting in enhanced mid-latitude plasma density basin.

230 2.2 In-situ: Ionosphere

231 The longevity of the density structures was favorable for frequent low orbiting space-
 232 craft flybys. We utilized measurements from the Defense Meteorological Satellite Pro-
 233 gram (DMSP), to characterize the mid-latitude ionosphere in Figure 6. We exploited the
 234 magnetic conjugacy of the MDS, in that we used measurements from southern and mapped
 235 them to the northern hemisphere. We use a mapping altitude of 350 km (the altitude
 236 used in constructing the TEC maps), using the Apex model of the geomagnetic field (Emmert
 237 et al., 2010). DMSP probed the topside ionosphere at ~ 860 km, measuring ion density,
 238 composition, temperature, drift, and electron temperature. Note that electron temper-
 239 ature from F18 is removed due to problems with the Langmuir probe. Secondly, the ion
 240 drift meter aboard F17 has baseline issues, therefore cross-track (v_y) and vertical (v_z)
 241 ion drift amplitudes are not calibrated. The measurements, however, are valid as guid-
 242 ance for direction and relative trend. All ion drift velocities are in the Earth's rotational
 243 frame of reference. Resolved vectors of horizontal ion drift (from ram velocity v_x , and
 244 cross-track v_y) are in geographic coordinates and plotted along the DMSP trajectories
 245 in Figures 6a-f. The region of the mid-latitude trough ($T0$) is magenta shaded, whereas
 246 the area around the MDS is shaded in green.

247 The first DMSP pass (D1) in Figure 6a by the F16 satellite probed the American
 248 ionosphere sector right at the time of the first impulsive drop of the SYM/H. The hor-
 249 izontal flow vectors indicate the presence of a strong (~ 1.6 km/s) SAPS flow that peaked
 250 at the trough equatorward boundary (53° MLAT), and it penetrated down to $\sim 40^\circ$ MLAT.
 251 The sunward flow was associated with an upflow, reaching at ~ 800 m/s, and extended
 252 equatorward for $\sim 2^\circ$. Then, the F18 (D2) passed right through an early stage of devel-
 253 oping MDS. Figure 6b shows an outstanding ion flow channel associated and elongated
 254 along the $P1$ plume poleward boundary, as well as flow perturbations positively corre-
 255 lated with the other density perturbations within the MDS. Besides, the D2 time series
 256 plot reveals a non-uniform trough $T1$. Additionally, initial perturbations in ion temper-
 257 ature (Ti) are measured along with the MDS which are in quadrature with the density
 258 perturbations. The background Ti within the $P1$ plume was at about 1,200 K, whereas
 259 a subtle increase in $Ti \sim 1,500$ K was measured within density the depletions. Vertical
 260 lines in the time-series plot highlight positive correlation between density and flow, and
 261 negative correlation with Ti.

262 The next flybys occurred an hour after the last impulsive event (event (3)), at a
 263 time the MDS were fully developed. First, the F16 (D3) traversed over the western United
 264 States, over the region where the MDS were entrained by the SAPS and hence parallel
 265 with the mid-latitude trough ($T0$). The F16 measured unperturbed SAPS flow encom-
 266 passing both the $T0$ trough and the MDS down to 40° MLAT. Vertical drift was neg-
 267 ligible. At that time, electron density perturbations within the MDS were already highly

268 structured, maintaining characteristic enhancements at either side of the secondary trough
 269 $T1$. Electron temperature (T_e) was profoundly increased within both troughs.

270 Lastly, F17 in D4 pass traversed the area around 2:30 UT, at a time the MDS where
 271 already dissipating and the secondary $T1$ trough was reforming into the density holes.
 272 Fortuitously, the F17-D4 passed across the MDS where there was substantially wider stand-
 273 off distance to the main $T0$ trough. The F17 measured horizontal ion convection rever-
 274 sal in the adjacent troughs. As explained above, the F17 ion drift meter was not cali-
 275 brated and thus the amplitude of the flow is ambiguous. The region of the MDS was still
 276 associated with a distinct increase in the temperatures. Both T_e and T_i were distinctly
 277 elevated, both near the secondary trough $T1$, and the plume $P2$ that separated both troughs.

278 In aggregate, the in-situ measurements show that the density plume $P1$ and the
 279 trough $T1$ are associated with flow channels, whereas no distinct ion flows were measured
 280 above the trough $T2$. The $T2$ trough was present at the very beginning of the MDS for-
 281 mation, identified in the ΔTEC maps, however, it could also appear as an optical fea-
 282 ture due to density enhancement $P1$. We lack crucial in-situ measurement at the time
 283 of the initial break up, around 09/07-23:30 UT (cf. Figure 3) when its presence was very
 284 clear. A strong ion flow along the $P1$ - $T1$ boundary, reversed at $\sim 2:00$ UT. There is no
 285 consistent pattern in the vertical ion flow; first, there was an upflow (until D3, 01:15UT),
 286 followed by a downflow above the MDS. Temperature measurements, however, show a
 287 persuasive electron and ion temperature increase co-located with density decrease. Lastly,
 288 ion density profiles indicate an increase of small scale irregularities within the MDS over
 289 time.

290 2.3 In-situ: Magnetosphere

291 The Radiation Belt Storm Probe A (RBSP-A) crossed the American longitude sec-
 292 tor during an inbound flight during the MDS developing phase. Figure 7 shows selected
 293 measurements with derived quantities. Figure 7A consists of in-situ measurements of the
 294 electric field, high-frequency radio (HFR) spectra, and ion energy flux (high and low en-
 295 ergy). The ionospheric footprint of the RBSP-A trajectory, with a modulated electric
 296 field measurement, is depicted in Figure 7C. The upper-hybrid (f_{uh}) emission, a contin-
 297 uous narrow-band line in the HFR spectra, is used to find the density structure. RBSP-
 298 A was first located outside the plasmasphere until $\sim 23:30$ UT. It then entered the plas-
 299 masphere. However, the plasmopause was not a single boundary, but rather the satel-
 300 lite encountered multiple density gradients. This is consistent with the structured den-
 301 sity observed at the equatorward boundary of the main trough. The low-density region
 302 at $\sim 23:48$ UT contains a highly fluctuating electric field, which could be the SAPS wave
 303 structure (SWS) (E. V. Mishin et al., 2003). The spacecraft then traversed the plasma-
 304 spheric signature of the MDS.

305 The electric field measurements come from the Electric Field and Wave (EFW) in-
 306 strument (Wygant et al., 2013), which is measured in the antenna frame of reference (x' ,
 307 y' , z'). The spin-plane components ($E_{y'}$, $E_{z'}$) are measured directly. The component along
 308 the antenna boresight (x') cannot be measured, but is obtained assuming zero parallel
 309 electric field. We then convert the electric field to the Solar Magnetic (SM) coordinates
 310 (x , y , z). The SM electric field components are plotted in Figure 7A1. A large double
 311 hump increase in the E_x (~ 20 mV/m) was observed at 00:25 UT, $L \sim 1.9$, 19:00 MLT.
 312 The negative E_x component of electric field designates eastward direction in the mag-
 313 netic equatorial plane, at dusk local time sector. The resulting $\mathbf{E} \times \mathbf{B}$ drift is upward and
 314 poleward along magnetic field lines. At the same time, E_y component of the electric field,
 315 pointing duskward/outward, shows correlated but smaller enhancements causing west-
 316 ward tilt in the resulting $\mathbf{E} \times \mathbf{B}$ drift. Ionospheric projection of the drift is therefore pole-
 317 ward and westward, just as measured by the DMSP-D2 pass.

318 The HFR spectra show a sharp decrease (within the MDS shading) at a location
 319 between the E_x spikes. The measured positions of the MDS are marked on the HFR spec-
 320 tra. The upper-hybrid frequency f_{uh} changed from $\sim 10^3$ Hz to ~ 500 Hz from density
 321 plume $P1$ to the trough $T1$. That roughly corresponds to plasma density change from
 322 $12,300 \text{ cm}^{-3}$ to 3000 cm^{-3} . Notably, another sharp density trough was measured over
 323 the Atlantic, at $L=1.5$, 21 MLT (68°W , 22°N), a possible signature of another trough
 324 ($T3$).

325 An enhancement of ~ 100 keV ion flux (Figure 7A3) was measured by the radia-
 326 tion belt storm probe ion composition experiment (RBSPICE) (Mitchell et al., 2013).
 327 The high-energy ion flux penetrated down to $L \approx 2.3$ at 18 MLT. The earthward edge
 328 of high energy ions coincided with and increase in plasma density, that correspond to
 329 the secondary plume $P1$. The fiducial blue line is the RBSPICE-derived perpendicular
 330 ion pressure (P_\perp), showing a continuous gradient up to the edge of data collection. No-
 331 tably, the first E_x intensification lies within the pressure gradient with a value ~ 1 nPa.
 332 Lower energy (< 50 keV) ion flux (Figure 7A4) from the Helium, Oxygen, Proton, and
 333 Electron (HOPE) instrument (Funsten et al., 2013) show increased > 10 keV flux, con-
 334 tinuously extending the RBSPICE measurements. In the area of the MDS, there were
 335 some periodic enhancements in the ~ 100 eV energy range. Comparing three consecu-
 336 tive orbits (panel B), we identify the ion flux enhancements in the RBSPICE and HOPE
 337 data are due to ring current injections, at times of the storm main phase, and substorm
 338 injections.

339 Mapping the RBSP-A measurements to the ionosphere puts the magnetospheric
 340 observations into the ionospheric perspective in Figure 7C. The trajectory thickness rep-
 341 represents the electric field magnitude, while the color indicates the strength and direction
 342 of its zonal component E_x . Big oscillations in the electric field magnitude, most likely
 343 the SWS, map poleward of the trough equatorward boundary, into the SAPS channel.
 344 There is no direct evidence showing SWS to have any connection with the MDS. The
 345 most significant observation, however, is the ionospheric location of the anomalous elec-
 346 tric field increases near the MDS. The double-hump increase is located at the bound-
 347 aries of the ionospheric secondary trough $T1$, which implies the magnetospheric in-situ
 348 plasma density fluctuations with the MDS observed in the ionosphere. The double hump
 349 electric field is located near $L=1.9$ (45° MLAT), with an apex height of > 5700 km. Be-
 350 cause $T1$ and the in-situ density local minimum were seen on the same L-shell, the re-
 351 duced density is not localized ionospheric feature, in fact, it extends to the plasmasphere
 352 along the magnetic field line. The secondary trough $T1$ extends poleward in the iono-
 353 sphere up to 51° MLAT ($L=2.4$) at that time, which would map to 8900 km in the equa-
 354 torial plane. We treat the magnetosphere-ionosphere system as electrostatic, the iono-
 355 spheric trough with associated electrostatics span from the equatorial ionosphere up
 356 to the trough equatorward boundary at $L=2.4$, 19:00 MLT both in the ionosphere and
 357 magnetosphere. Just like the historical observations made by Brace et al. (1974).

358 Lastly, we utilize the International Geomagnetic Reference Field (IGRF)-12 geo-
 359 magnetic field model (Thébault et al., 2015), and electric field mapping scaling factors
 360 (Mozer, 1970), to compute magnitudes of $\mathbf{E} \times \mathbf{B}$ drift ($V'_{E \times B}$) from the RBSP-A at the
 361 DMSP altitude (850 km). In particular, we compare the estimated drift to the drift mea-
 362 sured by the DMSP F18-D2, which probed the MDS 30 minutes earlier in Figure 8. The
 363 DMSP drift speed at the density enhancement ($P1$) gradient peaked at 1.6 km/s and
 364 reduced to ~ 500 m/s in the adjacent trough ($T1$). The estimated ionospheric drift from
 365 the RBSP-A ($V'_{E \times B}$) reached 1.3 km/s at the $P1-T1$ boundary, and 1.6 km/s at the
 366 other boundary. The $V'_{E \times B}$ within the trough was ~ 400 m/s. Conjugate spacecraft ob-
 367 servations directly show the electric field associated features as well as density structure
 368 maps along field lines. The RBSP observations thus support the interpretation that the
 369 electric field structure driving the flow along the MDS forms as a result of the magnetosphere-
 370 ionosphere coupling, as it resided within the earthward ring current pressure gradient

371 region. Hence, the resulting ionospheric trough was likely driven by transport and re-
 372 combination in the ionosphere (e.g., Schunk et al., 1976).

373 **3 Discussion**

374 We characterize the mid-latitude density striations, discuss possible driving mech-
 375 anisms, and put them in context with historical observations. Specifically, we focus on
 376 mid-latitude density plumes $P1$ and $P2$, and the secondary mid-latitude trough $T1$ sep-
 377 arating them. The other trough, $T2$ identified in the TEC maps shows no associated flow
 378 channels in the in-situ measurements, thus we cannot link it to a geophysical source. Sim-
 379 ilarly, the trough $T3$ from the RBSP-A HFR spectra lack ionospheric measurements. Ev-
 380 ery aspect of the observed mid-latitude phenomenon is intriguing and important for the
 381 space weather, however, we focus our discussion and further analysis only to the MDS
 382 development phase, up to the point the MDS began to dissipate. The dissipation and
 383 reconfiguration of the MDS require a separate study of its own.

384 **3.1 EPB Hypothesis**

385 From a GPS-TEC map point of view, the MDS appear to have a base at low lat-
 386 itude ionosphere, and then expand poleward, as it was first suggested by Aa et al. (2019).
 387 In addition, historical in-situ observations of similar (likely identical), mid-latitude phe-
 388 nomenon (Brace et al., 1974; Greenspan et al., 1991; J. C. Foster & Rich, 1998; C.-s. Huang
 389 et al., 2007), were inclined towards the EPB hypothesis. However, the historical stud-
 390 ies lacked spatial context. Our study now provided comprehensive structure and evolu-
 391 tion of the MDS by the GPS-TEC maps, contemporary high resolution convection maps
 392 and unprecedented spacecraft conjunctions.

393 Let's consider the possibility of extreme EPB expansion, starting with the estab-
 394 lished spatiotemporal morphology attributed to mid-latitude EPB (i.e., Ma & Maruyama,
 395 2006; Martinis et al., 2015). In their cases, a poleward expansion of the EPB is evident
 396 by means of airglow depletion and irregularity maps. Additionally, their signatures were
 397 progressively more structured at higher latitudes, indicative of the topside non-linear bub-
 398 ble decay, such as bifurcation. Irregularity maps from recent studies (Aa et al., 2019; Za-
 399 kharenkova & Cherniak, 2020) show rather uniform pattern along density depletions, con-
 400 trary to the expected reduction with latitude. Interestingly, the DMPS F18-D2 directly
 401 measured density perturbations about 30 minutes before ground-based measured irreg-
 402 ularities (cf., Aa et al., 2019; Zakharenkova & Cherniak, 2020). The initial irregular-
 403 ities, however, became highly irregular later, just like in the historical cases (Brace et
 404 al., 1974; J. C. Foster & Rich, 1998; Greenspan et al., 1991; C.-s. Huang et al., 2007).

405 The MDS were associated with flow channels, which we discuss in the context of
 406 the underlying density perturbations. Elevated ion drifts have been surveyed within EPBs
 407 (i.e., C.-S. Huang et al., 2010), but with significant differences in magnitude and mor-
 408 phology compared with the current event. Ion drifts within an EPB peak in the center
 409 and gradually decreases toward edges. In contrast, the ion drifts measured within the
 410 MDS peak at the trough's boundary with a magnitude of ~ 5 greater than those observed
 411 within EPB's. Observations of supersonic drifts inside EPBs (e.g., Aggson et al., 1992)
 412 were observed, however within the EPB seed at the magnetic equator. The opposite mor-
 413 phology in flow pattern was measured both by the DMPS and the RBSP-A, 30 minutes
 414 apart. Lastly, an electrodynamic feature of the EPB is a current system that causes mag-
 415 netic field deflection δB in in-situ probes, with deflections of an order of nT (Rodríguez-
 416 Zuluaga & Stolle, 2019). The DMSP did not measure any magnetic field perturbations
 417 during the flybys over the MDS (hence, not shown here). The magnetometer onboard
 418 DMSP has a resolution of 2 nT.

419

3.2 Penetration Electric Field

420

421

422

423

424

425

426

427

428

429

430

431

432

433

434

435

436

437

The MDS began to emerge at the storm onset, near the PT, just east to Florida, United States. The eastward electric field at low latitudes accelerates poleward plasma transport due to combined effects of the PEF, the polarization electric field at the sunset terminator (PT effect), and the reduced magnetic field strength in the vicinity of the SAA. Further, magnetic declination imposes an additional westward component in the Atlantic longitude sector. The result is a basin of dense plasma at lower mid-latitudes, close to Florida (J. Foster & Erickson, 2013), that is magnetically conjugate (J. C. Foster et al., 2007), and leaves a void in the night time equatorial ionosphere (Immel et al., 2005). The PEF was present in the equatorial region for ~ 5 hours, with two prominent intensifications. As the mid-latitude density plumes, $P1$ and $P2$ were developing during that time. The $P1$ plume was specifically dense and elongated, located near the PT. Its rapid and localized enhancement is consistent with numerous observations of extreme plasma uplift during prompt PEF intensifications (Kil et al., 2007). Conversely, the second $P2$ density plume is mysterious as it was entirely located in the nightside ionosphere. As the TEC maps showed a completely empty equatorial ionosphere in the nightside, the source of the $P2$ plume should have been poleward plasma transport from lower latitudes. The eastward directed disturbance dynamo electric field in the nightside (Blanc & Richmond, 1980) could have provided the driving electric field.

438

3.3 Trough Morphology

439

440

441

442

443

444

445

446

447

448

449

450

451

452

453

454

455

The secondary trough $T1$, on the other hand, cannot be explained by any of the ionospheric low latitude mechanism except for an EPB, and plasma downflow (measured upflow). As discussed earlier, the measured electrodynamic pattern does not agree with the EPB fundamentals. Instead, we argue that a progressive development accompanied by steep gradients is a characteristic of convection and recombination driven mid-latitude trough (e.g., Moffett & Quegan, 1983, and references therein). The convection there was driven by the imposed electric field originating at the ring current earthward boundary (Goldstein et al., 2005; Toffoletto et al., 2003), as measured by the RBSP-A. This secondary trough, just like the ordinary mid-latitude trough, was initially carved by the magnetospheric electric field, which was then maintained by the polarization electric field via the resulting conductance gradient in the ionosphere. Hence, such a trough persists for a long period of time after the initial driver dies off (Moffett & Quegan, 1983; Shinbori et al., 2018). Interestingly, the initial location of the peak ion drift was located at the trough's gradients. Nevertheless, convection-driven recombination can account for the progressive erosion observed along with the MDS. Ultimately, the recombination is faster in a region of the denser plasma, hence the faster trough depletion at lower latitudes.

456

457

458

459

460

461

462

463

464

465

466

467

The secondary trough $T1$ exhibits similar ionospheric properties (plasma density profile, temperatures, temporal evolution), but with strikingly different spatial extent. The spatial extent based on the observations was confined to the dusk-evening sector, connecting the equatorial ionosphere with high latitudes. The total spatial extent, however, cannot be unambiguously determined due to the lack of observations over the Atlantic and Pacific sectors. The secondary trough reached a width of ~ 300 km (before dissipation), with a minimum TEC of ~ 3 TECu, (in-situ density similar to the main trough), an electron temperature increase by a factor of 2 (with respect to the denser mid-latitude plasma) and an ion temperature increase (lagging the electron temperature increase), very similar to the observations by Brace et al. (1974). The horizontal ion drift reached values of ~ 1.5 km/s (calibrated F16, and F18). The horizontal drift has a conjugate electric field intensification at the ring current pressure gradient near the equatorial plane.

468

3.4 Current Interpretation

469

470

471

472

473

474

475

476

477

478

479

480

While plasma enhancements appear to be a transport effect, the troughs, on the other hand, need an alternative explanation. Interestingly, the $P1$ plume started developing just west of the PT, but, it did not surf the PT, in contrast to the event studied by J. Foster and Erickson (2013). Instead, its low latitude base extended into the night-side. Additionally, the plume became highly elongated (extended poleward and westward), similar to the SED plume in the presence of the strong adjacent SAPS flow (J. C. Foster, 1993). A similar situation was measured in this event when a $>1\text{km/s}$ flow guided a plume sunward, but with a drastically different spatial figure. While the SED plume is an ionospheric manifestation of the plasmaspheric drainage plume (Foster, J C, P.J. Erickson, A.J. Coster, J. Goldstein, 2002), the secondary plume $P1$ could as well be a manifestation of another plasmaspheric feature ("dusk horn") (cf. Goldstein et al., 2005), as we provide in-situ evidence for plasmaspheric density structures.

481

482

483

484

485

486

487

488

489

490

491

492

493

494

495

496

497

SuperDARN maps, as well as the RBSP-A observations, provided a global context of the system response. While the magnetospheric observations provide important insight into the MDS field-aligned characteristics, it is intriguing to observe high latitude convection distortion in sync with the mid-latitude plasma restructuring. The equatorward flow excursions measured by the SuperDARN could be coincidental, however, they persisted for more than 30 minutes in the time of the MDS development. Unfortunately, SuperDARN did not directly measure the flow within the MDS, although it did measure perturbed high-latitude convection just poleward of the MDS. Hence, the causal relationship remains ambiguous. Nevertheless, plausible speculation is that the MDS are a product of a global geospace response, due to a competition of low- and high-latitude electrodynamics. On one hand, there was a long-lasting presence of the eastward electric field at low latitudes (e.g., C.-s. Huang et al., 2005): the PEF during the storm onset and the consecutive substorm injections, and disturbance dynamo at later times – in the nightside ionosphere. Also, the magnetogram provides evidence for an abrupt PEF enhancement, similar to localized enhancements measured in-situ (Kil et al., 2007). Enhanced flow channel with a conjugate electric field enhancement did exist in the inner magnetosphere located in the vicinity of the ring current injection.

498

499

500

501

502

503

504

505

506

507

508

509

510

511

512

513

514

515

While the source of the MDS formation is still somewhat speculative, we find firm evidence that the MDS are a product of magnetosphere-ionosphere coupling by virtue of conjugate DMSP-RBSP plasma observations. It is highly unlikely for an ionospheric mechanism to produce 1.6 km/s flow at mid-latitudes, which would require an eastward electric field of $\sim 50\text{ mV/m}$ at DMSP heights. This electric field, ultimately, resided within the ring current pressure gradient. Supersonic flows at the DMSP altitudes were measured, but only at the equator, within the base of an EPB (i.e., Aggson et al., 1992). In contrast, we find it plausible that the MDS could arise as a consequence of modified electrodynamics associated with extreme ring current injection, but displaced to the dusk local time sector. The time scale of the modification was rapid and accompanied by rotational, and enhanced ionospheric flows measured by the SuperDARN. The distorted flow measured by the SuperDARN agrees well with a model of substorm injection modeled by Yang et al. (2012). A substorm modification of the ionospheric electrodynamics reaching equatorial regions is a well-known phenomenon (Kikuchi et al., 2010; Ebihara et al., 2014; Hashimoto et al., 2017). These studies emphasized its impacts on the modified mid-latitude electric field, as well as modulation of mid-latitude convection by vortex-like flows. Nevertheless, such extreme consequences to mid-latitude density modulation have not yet been demonstrated.

516

4 Conclusions

517

518

We have presented observations and analysis of the MDS, anomalous plasma density modulation of the storm enhanced density. We have characterized the density stri-

519 ations by virtue of remote and in-situ observations in unprecedented detail. We find that
 520 the MDS developed progressively, with seed density perturbations in place prior to the
 521 later irregularities. The development took place in the midst of successive impulsive events
 522 involving prompt PEF, and episodic auroral electrojet intensifications. We summarize
 523 the observations with a pictorial illustration in Figure 9, where we build upon the sketch
 524 of Brace et al. (1974) . The illustration consists of two projections. First, the meridional
 525 cut near 19 MLT, at 1:00 UT, illustrates the density striations within and near the plasma-
 526 pause boundary. The other projection illustrates the local time radial dependence of the
 527 density striation. The MDS cut through the EIA and were wrapped around the SED at
 528 mid-latitudes. The MDS consist of a series of troughs and plumes within the plasma-
 529 sphere. The illustration does not include the plausible existence of another density trough
 530 *T3*, measured by the RBSP-A. We find that the MDS are positively correlated with plasma
 531 flows. We find that the electric field peaks at density gradients, making them distinct
 532 from the main mid-latitude trough as well as the EPB. In addition, the measurements
 533 show isolated plasma temperature enhancements from the main mid-latitude trough. Lastly,
 534 the mid-latitude density striations with co-located electric field perturbations in the equa-
 535 torial plane were located just earthward of the <200 keV ring current ion injection, still
 536 in the region of the ion pressure gradient.

537 We put the observations into the historical perspective, and discuss possible geo-
 538 physical drivers. The MDS developed during the period of the enhanced eastward elec-
 539 tric field, near the polarization terminator. However, highly localized development of den-
 540 sity structures deviated from the ordinary. The density enhancements, specifically the
 541 plume *P1*, show a characteristic nature of poleward and westward transport guided by
 542 the adjacent flow channel. A PEF by itself cannot produce such localized density as it
 543 would imply the PEF itself had dramatic zonal structure. Therefore, we argue that an-
 544 other source of the electric field perturbed the dusk region of the ionosphere, which re-
 545 sulted as a coherent sequence of density perturbations with associated flow channels. We
 546 identified a sequence of impulsive events with characteristic electric field modifications
 547 that likely served as the source of initial flow channels. In particular, crucial in-situ ob-
 548 servations of magnetospheric plasma indicated the location of the electric field within
 549 the ring current pressure gradient.

550 Acknowledgments

551 The study was supported by NSF-AGS 1821135, NSF-AGS-1907698, NASA-0NSSC18K0657,
 552 and AFOSR FA9559-16-1-0364 awards to Boston University. The GPS TEC data, SYM/H
 553 and Kp indices are available on <http://millstonehill.haystack.mit.edu/>. Solar wind data
 554 and electrojet indices were taken from https://omniweb.gsfc.nasa.gov/form/omni_min.html.
 555 DMSP and SuperDARN data are currently available at <http://cedar.openmadrigal.org>
 556 and <http://vt.superdarn.org/>.

557 References

- 558 Aa, E., Huang, W., Liu, S., Ridley, A., Zou, S., Shi, L., ... Wang, T. (2018,
 559 mar). Midlatitude Plasma Bubbles Over China and Adjacent Areas Dur-
 560 ing a Magnetic Storm on 8 September 2017. *Space Weather*, 16(3), 321–
 561 331. Retrieved from <http://doi.wiley.com/10.1002/2017SW001776> doi:
 562 10.1002/2017SW001776
- 563 Aa, E., Zou, S., Ridley, A., Zhang, S., Coster, A. J., Erickson, P. J., ... Ren, J.
 564 (2019). Merging of Storm Time Midlatitude Traveling Ionospheric Distur-
 565 bances and Equatorial Plasma Bubbles. *Space Weather*, 17(2), 285–298. doi:
 566 10.1029/2018SW002101
- 567 Aggson, T. L., Burke, W. J., Maynard, N. C., Hanson, W. B., Anderson, P. C.,
 568 Slavin, J. A., ... Saba, J. L. (1992). Equatorial bubbles updrafting at
 569 supersonic speeds. *Journal of Geophysical Research*, 97(A6), 8581. doi:

- 570 10.1029/92ja00644
- 571 Anderson, D. (2002). Estimating daytime vertical ExB drift velocities in the equa-
 572 torial F-region using ground-based magnetometer observations. *Geophysical*
 573 *Research Letters*, *29*(12), 1596. Retrieved from [http://doi.wiley.com/](http://doi.wiley.com/10.1029/2001GL014562)
 574 [10.1029/2001GL014562](http://doi.wiley.com/10.1029/2001GL014562) doi: 10.1029/2001GL014562
- 575 Anderson, P. C., Hanson, W. B., Heelis, R. A., Craven, J. D., Baker, D. N., &
 576 Frank, L. A. (1993). A proposed production model of rapid subauroral ion
 577 drifts and their relationship to substorm evolution. *Journal of Geophysical*
 578 *Research: Space Physics*, *98*(A4), 6069–6078. doi: 10.1029/92ja01975
- 579 Anderson, P. C., Heelis, R. A., & Hanson, W. B. (1991). The ionospheric signatures
 580 of rapid subauroral ion drifts. *Journal of Geophysical Research*, *96*(A4), 5785.
 581 doi: 10.1029/90ja02651
- 582 Berdermann, J., Kriegel, M., Banyś, D., Heymann, F., Hoque, M. M., Wilken, V.,
 583 ... Jakowski, N. (2018). Ionospheric Response to the X9.3 Flare on 6 September
 584 2017 and Its Implication for Navigation Services Over Europe. *Space*
 585 *Weather*, *16*(10), 1604–1615. doi: 10.1029/2018SW001933
- 586 Blanc, M., & Richmond, A. (1980). The ionospheric disturbance dynamo. *Journal of*
 587 *Geophysical Research*, *85*(A4), 1669. Retrieved from [http://doi.wiley.com/](http://doi.wiley.com/10.1029/JA085iA04p01669)
 588 [10.1029/JA085iA04p01669](http://doi.wiley.com/10.1029/JA085iA04p01669) doi: 10.1029/JA085iA04p01669
- 589 Brace, L. H., Maier, E. J., Hoffman, J. H., Whitteker, J., & Shepherd, G. G. (1974,
 590 dec). Deformation of the night side plasmasphere and ionosphere during
 591 the August 1972 geomagnetic storm. *Journal of Geophysical Research*,
 592 *79*(34), 5211–5218. Retrieved from [http://doi.wiley.com/10.1029/](http://doi.wiley.com/10.1029/JA079i034p05211)
 593 [JA079i034p05211](http://doi.wiley.com/10.1029/JA079i034p05211) doi: 10.1029/JA079i034p05211
- 594 Bristow, W. A., Hampton, D. L., & Otto, A. (2016, feb). Highspatialresolution
 595 velocity measurements derived using Local DivergenceFree Fitting of Super-
 596 DARN observations. *Journal of Geophysical Research: Space Physics*, *121*(2),
 597 1349–1361. Retrieved from [https://onlinelibrary.wiley.com/doi/abs/](https://onlinelibrary.wiley.com/doi/abs/10.1002/2015JA021862)
 598 [10.1002/2015JA021862](https://onlinelibrary.wiley.com/doi/abs/10.1002/2015JA021862) doi: 10.1002/2015JA021862
- 599 Dimmock, A. P., Rosenqvist, L., Hall, J. O., Viljanen, A., Yordanova, E., Honko-
 600 nen, I., ... Sjöberg, E. C. (2019). The GIC and Geomagnetic Response
 601 Over Fennoscandia to the 78 September 2017 Geomagnetic Storm. *Space*
 602 *Weather*(MAY). doi: 10.1029/2018SW002132
- 603 Ebihara, Y., Tanaka, T., & Kikuchi, T. (2014, sep). Counter equatorial elec-
 604 trojet and overshielding after substorm onset: Global MHD simulation
 605 study. *Journal of Geophysical Research: Space Physics*, *119*(9), 7281–7296.
 606 Retrieved from <http://doi.wiley.com/10.1002/2014JA020065> doi:
 607 [10.1002/2014JA020065](http://doi.wiley.com/10.1002/2014JA020065)
- 608 Emmert, J. T., Richmond, A. D., & Drob, D. P. (2010). A computationally compact
 609 representation of magnetic-apex and Quasi-Dipole coordinates with smooth
 610 base vectors. *Journal of Geophysical Research: Space Physics*, *115*(8), 1–13.
 611 doi: 10.1029/2010JA015326
- 612 Foster, J., & Erickson, P. (2013, oct). Ionospheric superstorms: Polarization ter-
 613 minator effects in the Atlantic sector. *Journal of Atmospheric and Solar-*
 614 *Terrestrial Physics*, *103*, 147–156. Retrieved from [http://dx.doi.org/](http://dx.doi.org/10.1016/j.jastp.2013.04.001)
 615 [10.1016/j.jastp.2013.04.001](http://dx.doi.org/10.1016/j.jastp.2013.04.001)[https://linkinghub.elsevier.com/](https://linkinghub.elsevier.com/retrieve/pii/S1364682613001144)
 616 [retrieve/pii/S1364682613001144](https://linkinghub.elsevier.com/retrieve/pii/S1364682613001144) doi: 10.1016/j.jastp.2013.04.001
- 617 Foster, J. C. (1993, feb). Storm time plasma transport at middle and high latitudes.
 618 *Journal of Geophysical Research: Space Physics*, *98*(A2), 1675–1689. Retrieved
 619 from <http://doi.wiley.com/10.1029/92JA02032> doi: 10.1029/92JA02032
- 620 Foster, J. C., & Coster, A. J. (2007). Conjugate localized enhancement of total elec-
 621 tron content at low latitudes in the American sector. *Journal of Atmospheric*
 622 *and Solar-Terrestrial Physics*, *69*(10-11 SPEC. ISS.), 1241–1252. doi: 10.1016/
 623 [j.jastp.2006.09.012](http://doi.wiley.com/10.1016/j.jastp.2006.09.012)
- 624 Foster, J. C., & Rich, F. J. (1998, nov). Prompt midlatitude electric field effects

- 625 during severe geomagnetic storms. *Journal of Geophysical Research: Space*
 626 *Physics*, 103(A11), 26367–26372. Retrieved from [http://doi.wiley.com/](http://doi.wiley.com/10.1029/97JA03057)
 627 10.1029/97JA03057 doi: 10.1029/97JA03057
- 628 Foster, J. C., Rideout, W., Sandel, B., Forrester, W. T., & Rich, F. J. (2007).
 629 On the relationship of SAPS to storm-enhanced density. *Journal of At-*
 630 *mospheric and Solar-Terrestrial Physics*, 69(3), 303–313. doi: 10.1016/
 631 j.jastp.2006.07.021
- 632 Foster, J. C., & Vo, H. B. (2002). Average characteristics and activity dependence
 633 of the subauroral polarization stream. *Journal of Geophysical Research: Space*
 634 *Physics*, 107(A12), 1–10. doi: 10.1029/2002JA009409
- 635 Foster, J. C., Erickson, P. J., Coster, A. J., Goldstein, F. R. (2002, jan). Iono-
 636 spheric signatures of plasmaspheric tails. *Geophysical Research Letters*, 29(13),
 637 1623. Retrieved from <http://doi.wiley.com/10.1029/2002GL015067> doi:
 638 10.1029/2002GL015067
- 639 Funsten, H. O., Skoug, R. M., Guthrie, A. A., MacDonald, E. A., Balonado,
 640 J. R., Harper, R. W., ... Chen, J. (2013, nov). Helium, Oxygen, Proton,
 641 and Electron (HOPE) Mass Spectrometer for the Radiation Belt Storm
 642 Probes Mission. *Space Science Reviews*, 179(1-4), 423–484. Retrieved
 643 from <http://link.springer.com/10.1007/s11214-013-9968-7> doi:
 644 10.1007/s11214-013-9968-7
- 645 Goldstein, J., Burch, J. L., & Sandel, B. R. (2005). Magnetospheric model of sub-
 646 auroral polarization stream. *Journal of Geophysical Research: Space Physics*,
 647 110(A9), 1–10. doi: 10.1029/2005JA011135
- 648 Greenspan, M. E., Rasmussen, C. E., Burke, W. J., & Abdu, M. A. (1991, aug).
 649 Equatorial density depletions observed at 840 km during the great magnetic
 650 storm of March 1989. *Journal of Geophysical Research: Space Physics*, 96(A8),
 651 13931–13942. Retrieved from <http://doi.wiley.com/10.1029/91JA01264>
 652 doi: 10.1029/91JA01264
- 653 Hashimoto, K. K., Kikuchi, T., Tomizawa, I., & Nagatsuma, T. (2017). Substorm
 654 Overshielding Electric Field at Low Latitude on the Nightside as Observed
 655 by the HF Doppler Sounder and Magnetometers. *Journal of Geophysical Re-*
 656 *search: Space Physics*, 122(10), 10,851–10,863. doi: 10.1002/2017JA024329
- 657 Huang, C.-S., de La Beaujardiere, O., Pfaff, R. F., Retterer, J. M., Roddy, P. A.,
 658 Hunton, D. E., ... Rich, F. J. (2010, jul). Zonal drift of plasma particles
 659 inside equatorial plasma bubbles and its relation to the zonal drift of the bub-
 660 ble structure. *Journal of Geophysical Research: Space Physics*, 115(A7),
 661 1–12. Retrieved from <http://doi.wiley.com/10.1029/2010JA015324> doi:
 662 10.1029/2010JA015324
- 663 Huang, C.-s., Foster, J. C., & Kelley, M. C. (2005). Long-duration penetration
 664 of the interplanetary electric field to the low-latitude ionosphere during the
 665 main phase of magnetic storms. *Journal of Geophysical Research*, 110(A11),
 666 A11309. Retrieved from <http://doi.wiley.com/10.1029/2005JA011202> doi:
 667 10.1029/2005JA011202
- 668 Huang, C.-s., Foster, J. C., & Sahai, Y. (2007, may). Significant depletions of the
 669 ionospheric plasma density at middle latitudes: A possible signature of equato-
 670 rial spread F bubbles near the plasmapause. *Journal of Geophysical Research:*
 671 *Space Physics*, 112(A5), n/a–n/a. Retrieved from [http://doi.wiley.com/](http://doi.wiley.com/10.1029/2007JA012307)
 672 10.1029/2007JA012307 doi: 10.1029/2007JA012307
- 673 Immel, T. J., Foster, J. C., Coster, A. J., Mende, S. B., & Frey, H. U. (2005). Global
 674 storm time plasma redistribution imaged from the ground and space. *Geophys-*
 675 *ical Research Letters*, 32(3), 1–5. doi: 10.1029/2004GL021120
- 676 Kelley, M. C., Fejer, B. G., & Gonzales, C. A. (1979, apr). An explanation for
 677 anomalous equatorial ionospheric electric fields associated with a north-
 678 ward turning of the interplanetary magnetic field. *Geophysical Research*
 679 *Letters*, 6(4), 301–304. Retrieved from <http://doi.wiley.com/10.1029/>

- 680 GL006i004p00301 doi: 10.1029/GL006i004p00301
- 681 Kikuchi, T., Ebihara, Y., Hashimoto, K. K., Kataoka, R., Hori, T., Watari, S., &
682 Nishitani, N. (2010, may). Penetration of the convection and overshield-
683 ing electric fields to the equatorial ionosphere during a quasiperiodic DP
684 2 geomagnetic fluctuation event. *Journal of Geophysical Research: Space*
685 *Physics*, *115*(A5), n/a–n/a. Retrieved from [http://doi.wiley.com/10.1029/](http://doi.wiley.com/10.1029/2008JA013948)
686 [2008JA013948](http://doi.wiley.com/10.1029/2008JA013948) doi: 10.1029/2008JA013948
- 687 Kil, H., Oh, S.-J., Paxton, L. J., Zhang, Y., Su, S.-Y., & Min, K.-W. (2007, may).
688 Spike-like change of the vertical E B drift in the equatorial region during
689 very large geomagnetic storms. *Geophysical Research Letters*, *34*(9), 2–
690 5. Retrieved from <http://doi.wiley.com/10.1029/2007GL029277> doi:
691 [10.1029/2007GL029277](http://doi.wiley.com/10.1029/2007GL029277)
- 692 Lin, C. S., Yeh, H. C., & Chao, C. K. (2007). On a possible relationship between
693 density depletions in the SAA region and storm-enhanced densities in the con-
694 jugate hemisphere. *Journal of Atmospheric and Solar-Terrestrial Physics*,
695 *69*(1-2), 151–158. doi: 10.1016/j.jastp.2006.07.013
- 696 Ma, G., & Maruyama, T. (2006). A super bubble detected by dense GPS network at
697 east Asian longitudes. *Geophysical Research Letters*, *33*(21), 1–5. doi: 10.1029/
698 [2006GL027512](http://doi.wiley.com/10.1029/2006GL027512)
- 699 Martinis, C., Baumgardner, J., Mendillo, M., Wroten, J., Coster, A., & Paxton, L.
700 (2015). The night when the auroral and equatorial ionospheres converged.
701 *Journal of Geophysical Research A: Space Physics*, *120*(9), 8085–8095. doi:
702 [10.1002/2015JA021555](http://doi.wiley.com/10.1002/2015JA021555)
- 703 Mishin, E., Nishimura, Y., & Foster, J. (2017, aug). SAPS/SAID revisited: A causal
704 relation to the substorm current wedge. *Journal of Geophysical Research:*
705 *Space Physics*, *122*(8), 8516–8535. Retrieved from [http://doi.wiley.com/](http://doi.wiley.com/10.1002/2017JA024263)
706 [10.1002/2017JA024263](http://doi.wiley.com/10.1002/2017JA024263) doi: 10.1002/2017JA024263
- 707 Mishin, E. V., Burke, W. J., Huang, C. Y., & Rich, F. J. (2003). Electromagnetic
708 wave structures within subauroral polarization streams. *Journal of Geophysical*
709 *Research: Space Physics*, *108*(A8), 1–11. doi: 10.1029/2002JA009793
- 710 Mitchell, D. G., Lanzerotti, L. J., Kim, C. K., Stokes, M., Ho, G., Cooper, S., ...
711 Kerem, S. (2013, nov). Radiation Belt Storm Probes Ion Composition
712 Experiment (RBSPICE). *Space Science Reviews*, *179*(1-4), 263–308. Re-
713 trieved from <http://link.springer.com/10.1007/s11214-013-9965-x> doi:
714 [10.1007/s11214-013-9965-x](http://link.springer.com/10.1007/s11214-013-9965-x)
- 715 Moffett, R. J., & Quegan, S. (1983). The mid-latitude trough in the electron
716 concentration of the ionospheric F-layer: a review of observations and mod-
717 elling. *Journal of Atmospheric and Terrestrial Physics*, *45*(5), 315–343. doi:
718 [10.1016/S0021-9169\(83\)80038-5](http://doi.wiley.com/10.1016/S0021-9169(83)80038-5)
- 719 Mozer, F. S. (1970). Electric field mapping in the ionosphere at the equatorial plane.
720 *Planetary and Space Science*, *18*(2), 259–263. doi: 10.1016/0032-0633(70)90161
721 -3
- 722 Obana, Y., Maruyama, N., Shinbori, A., Hashimoto, K. K., Fedrizzi, M., Nosé, M.,
723 ... Shinohara, I. (2019). Response of the IonospherePlasmasphere Coupling to
724 the September 2017 Storm: What Erodes the Plasmasphere so Severely? *Space*
725 *Weather*(September 2017), 1–16. doi: 10.1029/2019sw002168
- 726 Piersanti, M., Di Matteo, S., Carter, B. A., Currie, J., & D’Angelo, G. (2019).
727 Geoelectric Field Evaluation During the September 2017 Geomagnetic
728 Storm: MA.I.GIC. Model. *Space Weather*, *17*(8), 1241–1256. doi:
729 [10.1029/2019SW002202](http://doi.wiley.com/10.1029/2019SW002202)
- 730 Rideout, W., & Coster, A. (2006, jul). Automated GPS processing for global tot-
731 tal electron content data. *GPS Solutions*, *10*(3), 219–228. Retrieved from
732 <http://link.springer.com/10.1007/s10291-006-0029-5>[http://files/](http://files/269/616882t7t21337t7.pdf)
733 [269/616882t7t21337t7.pdf](http://files/269/616882t7t21337t7.pdf) doi: 10.1007/s10291-006-0029-5
- 734 Rodríguez-Zuluaga, J., & Stolle, C. (2019). Interhemispheric field-aligned currents at

- 735 the edges of equatorial plasma depletions. *Scientific Reports*, 9(1), 1–8. doi: 10
736 .1038/s41598-018-37955-z
- 737 Schunk, R. W., Banks, P. M., & Raitt, W. J. (1976). Effects of Electric Fields and
738 Other Processes Upon the Nighttime High-Latitude F Layer. *J Geophys Res*,
739 81(19), 3271–3282. doi: 10.1029/JA081i019p03271
- 740 Shinbori, A., Otsuka, Y., Tsugawa, T., Nishioka, M., Kumamoto, A., Tsuchiya, F.,
741 ... Nishitani, N. (2018). Temporal and Spatial Variations of Storm Time
742 Midlatitude Ionospheric Trough Based on Global GNSS-TEC and Arase Satel-
743 lite Observations. *Geophysical Research Letters*, 45(15), 7362–7370. doi:
744 10.1029/2018GL078723
- 745 Thébault, E., Finlay, C. C., Beggan, C. D., Alken, P., Aubert, J., Barrois, O., ...
746 Zvereva, T. (2015). International geomagnetic reference field: The 12th gener-
747 ation international geomagnetic reference field - The twelfth generation. *Earth*,
748 *Planets and Space*, 67(1). doi: 10.1186/s40623-015-0228-9
- 749 Toffoletto, F., Sazykin, S., Spiro, R., & Wolf, R. (2003). Inner magnetospheric mod-
750 eling with the rice convection model. *Space Science Reviews*, 107(1-2), 175–
751 196. doi: 10.1023/A:1025532008047
- 752 Vierinen, J., Coster, A. J., Rideout, W. C., Erickson, P. J., & Norberg, J. (2016).
753 Statistical framework for estimating GNSS bias. *Atmospheric Measurement*
754 *Techniques*, 9(3), 1303–1312. doi: 10.5194/amt-9-1303-2016
- 755 Wygant, J. R., Bonnell, J. W., Goetz, K., Ergun, R. E., Mozer, F. S., Bale, S. D.,
756 ... Tao, J. B. (2013, nov). The Electric Field and Waves Instruments
757 on the Radiation Belt Storm Probes Mission. *Space Science Reviews*,
758 179(1-4), 183–220. Retrieved from [http://link.springer.com/10.1007/](http://link.springer.com/10.1007/s11214-013-0013-7)
759 [s11214-013-0013-7](http://link.springer.com/10.1007/s11214-013-0013-7) doi: 10.1007/s11214-013-0013-7
- 760 Yang, J., Toffoletto, F. R., Wolf, R. A., Sazykin, S., Ontiveros, P. A., & Weygand,
761 J. M. (2012, apr). Large-scale current systems and ground magnetic distur-
762 bance during deep substorm injections. *Journal of Geophysical Research: Space*
763 *Physics*, 117(A4), n/a–n/a. Retrieved from [http://doi.wiley.com/10.1029/](http://doi.wiley.com/10.1029/2011JA017415)
764 [2011JA017415](http://doi.wiley.com/10.1029/2011JA017415) doi: 10.1029/2011JA017415
- 765 Zakharenkova, I., & Cherniak, I. (2020, feb). When Plasma Streams Tie up Equato-
766 rial Plasma Irregularities with Auroral Ones. *Space Weather*, 18(2). Retrieved
767 from <https://onlinelibrary.wiley.com/doi/abs/10.1029/2019SW002375>
768 doi: 10.1029/2019SW002375

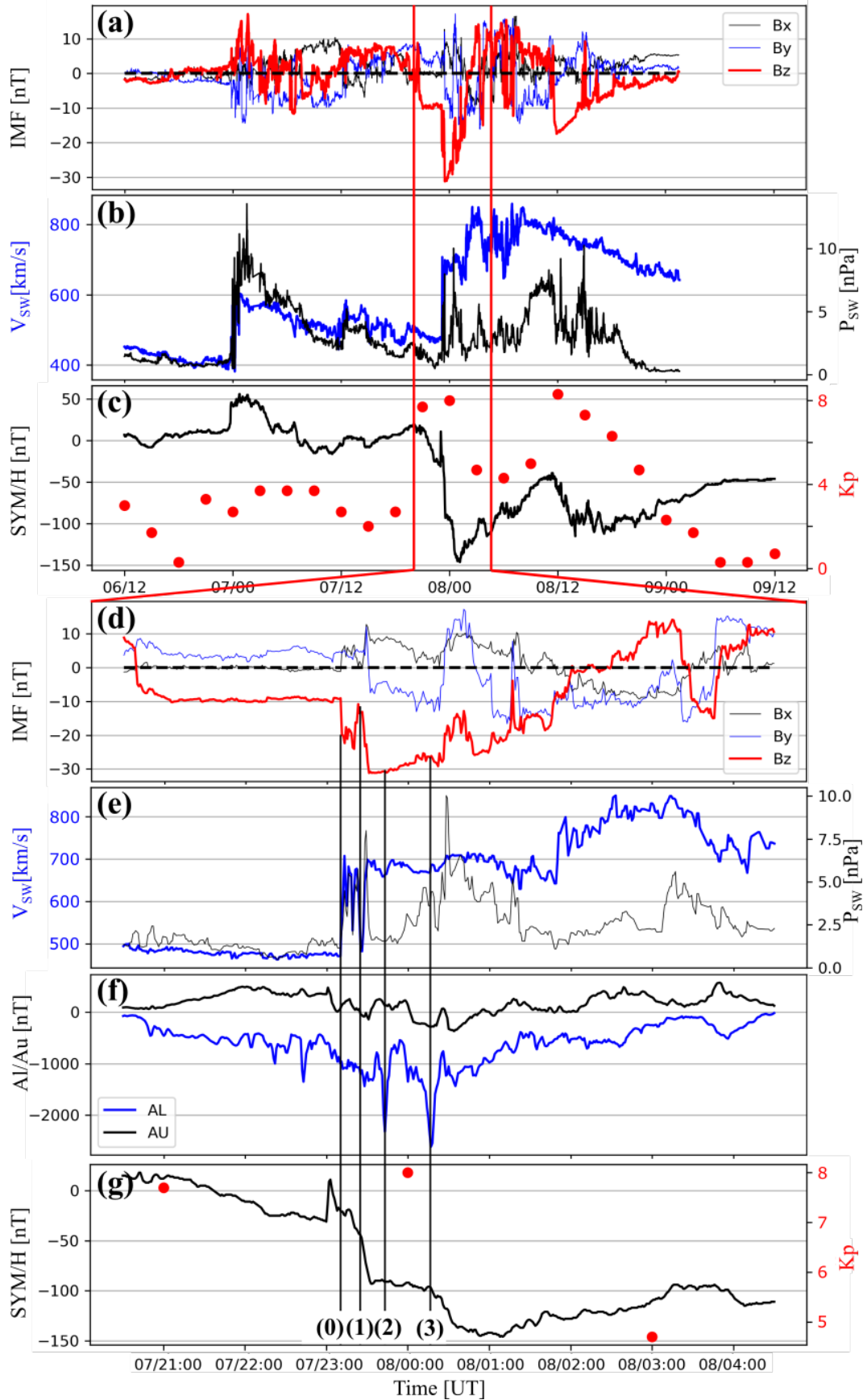


Figure 1. Solar wind and geomagnetic indices for the presented storm. (a-c) Solar wind and geomagnetic indices for a period of 3 days. (a) IMF in magnetospheric frame of reference (GSM); (b) Solar wind speed and pressure; (c) SYM/H index, and the 3-hour Kp index. (d-f) Zoomed in solar wind parameters with auroral electrojet indices for a time period of 9 hours. (d), (e), and (g) are a close up versions of upper panels; (f) Westward/Eastward (AL/AU) auroral electrojet indices.

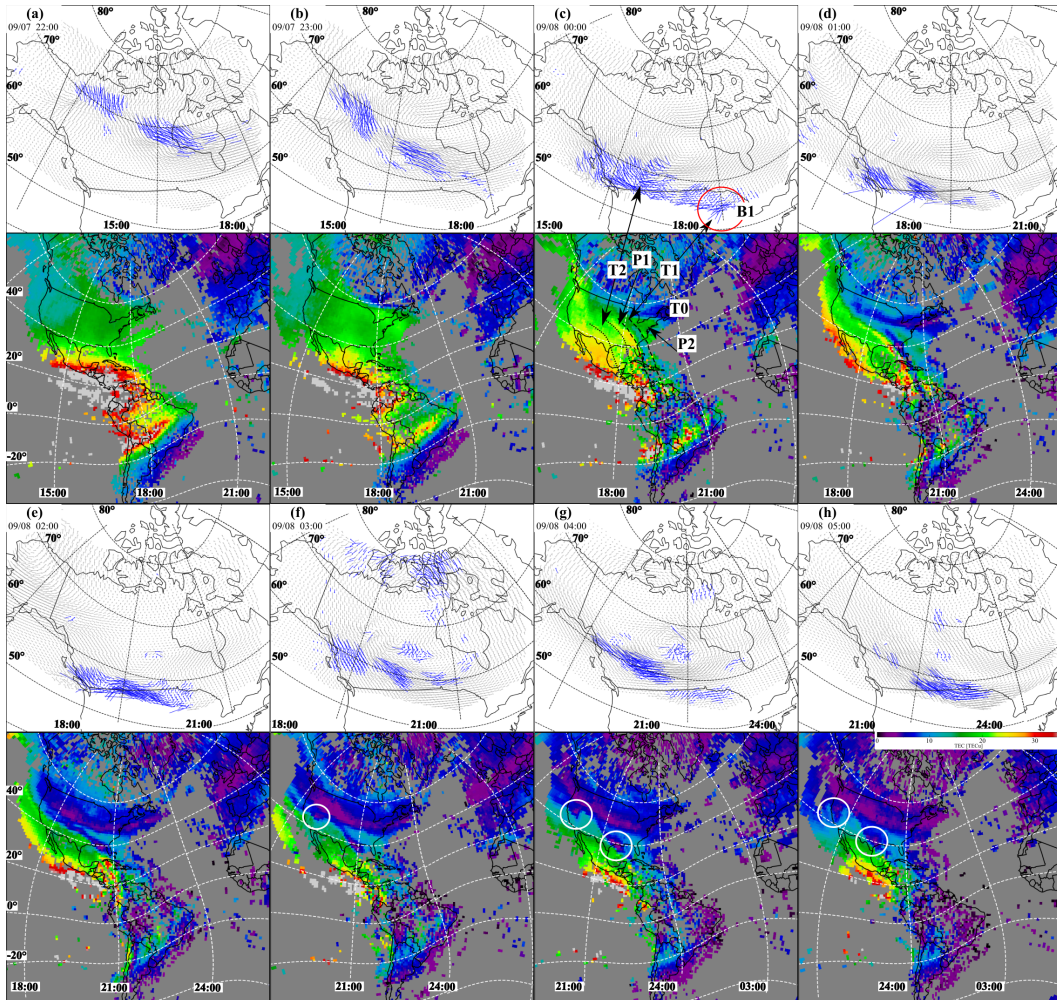


Figure 2. (a-h) Panels of high latitude convection and ionospheric TEC maps at 1 hour cadence. Each panel consists of: (top) SuperDARN convection maps using divergence-free fitting. Blue and gray vectors correspond to data points with and without radar echoes, respectively. (bottom) Global GPS TEC maps. White circles denote areas of density holes. Red circles denote location of high latitude convection breakups. Indicators are explained in text.

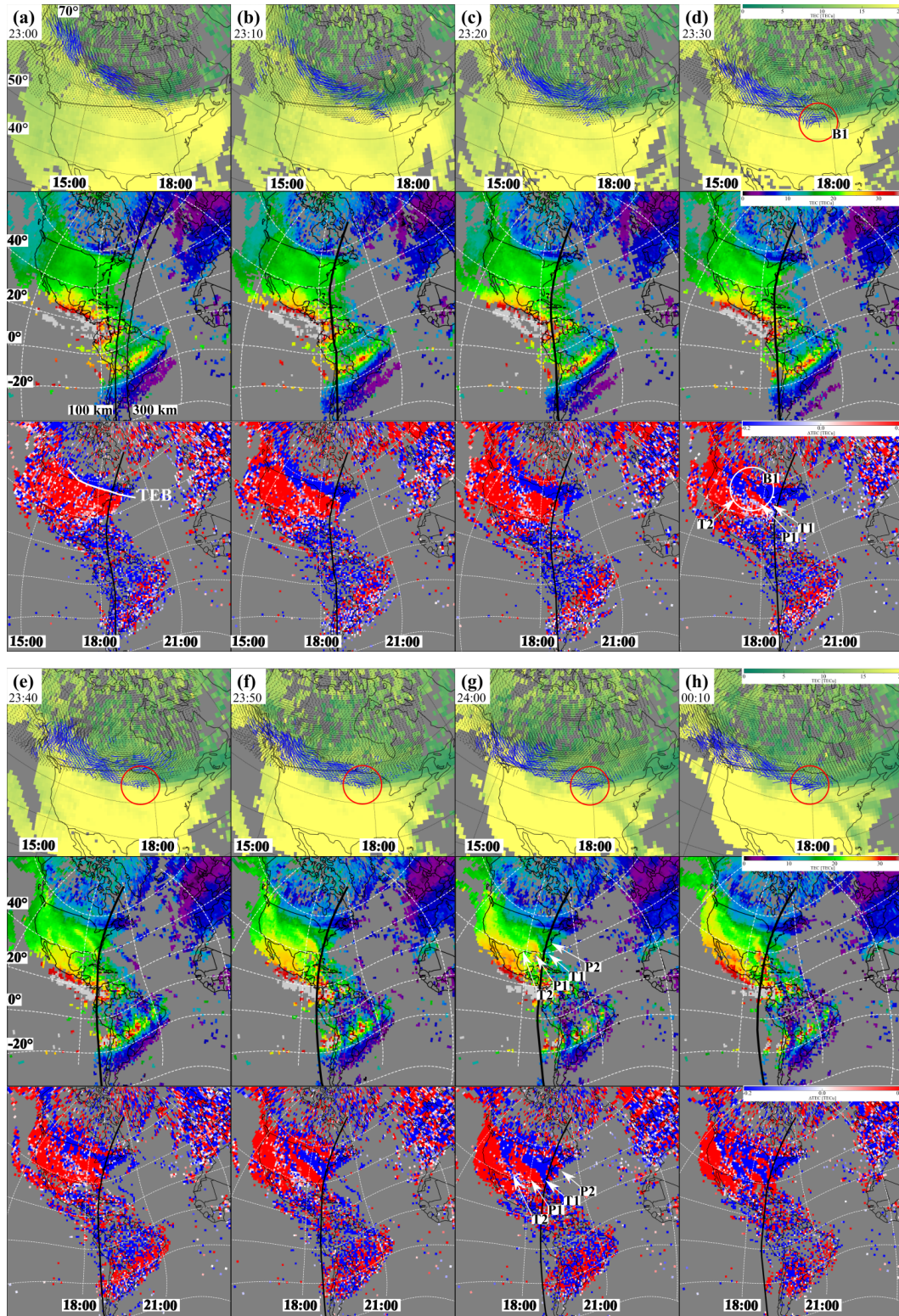


Figure 3. (a-h) Development of the MDS at 10 minute cadence. Each panel consists of: (top) SuperDARN convection on top of a GPS TEC map; (middle) GPS TEC map with a polarization terminator at 100 km. Panel (a) shows a sunset terminator at 100 km (thick) with projected conjugate terminator to northern hemisphere (dashed), and sunset terminator at 300 km (thin). Polarization terminator (PT) as defined in J. Foster and Erickson (2013) at 100 km is the bold thick in other panels; (bottom) Differential TEC maps with polarization terminator.

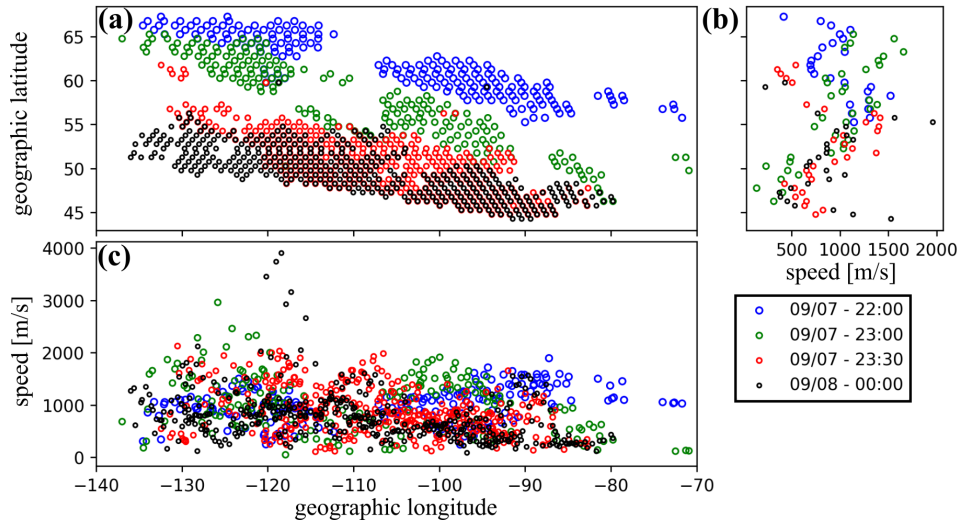


Figure 4. Backscatter-estimated SuperDARN locations and flows in geographic coordinates at four different times. (a) F-region backscatter geo-locations; (b) zonally averaged flow speed; (c) meridionally averaged flow speed.

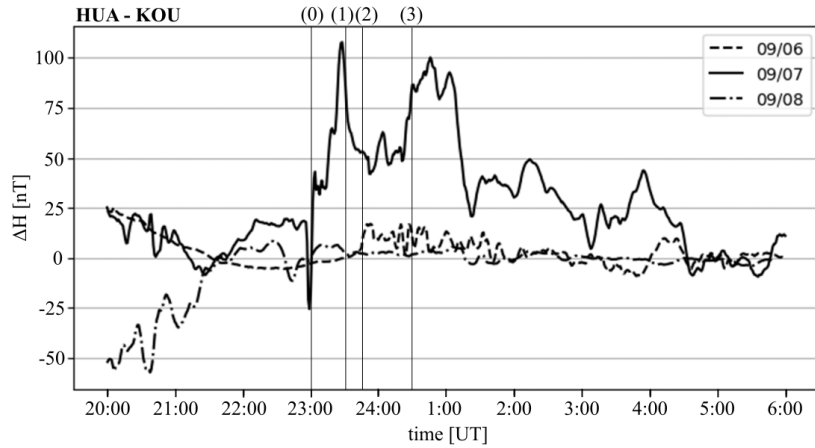


Figure 5. Equatorial electrojet measured by low latitude magnetometers from Huancayo (HUA) and Kourou (KOU) on three consecutive days at local times of the storm. Markers are defined with Figure 1.

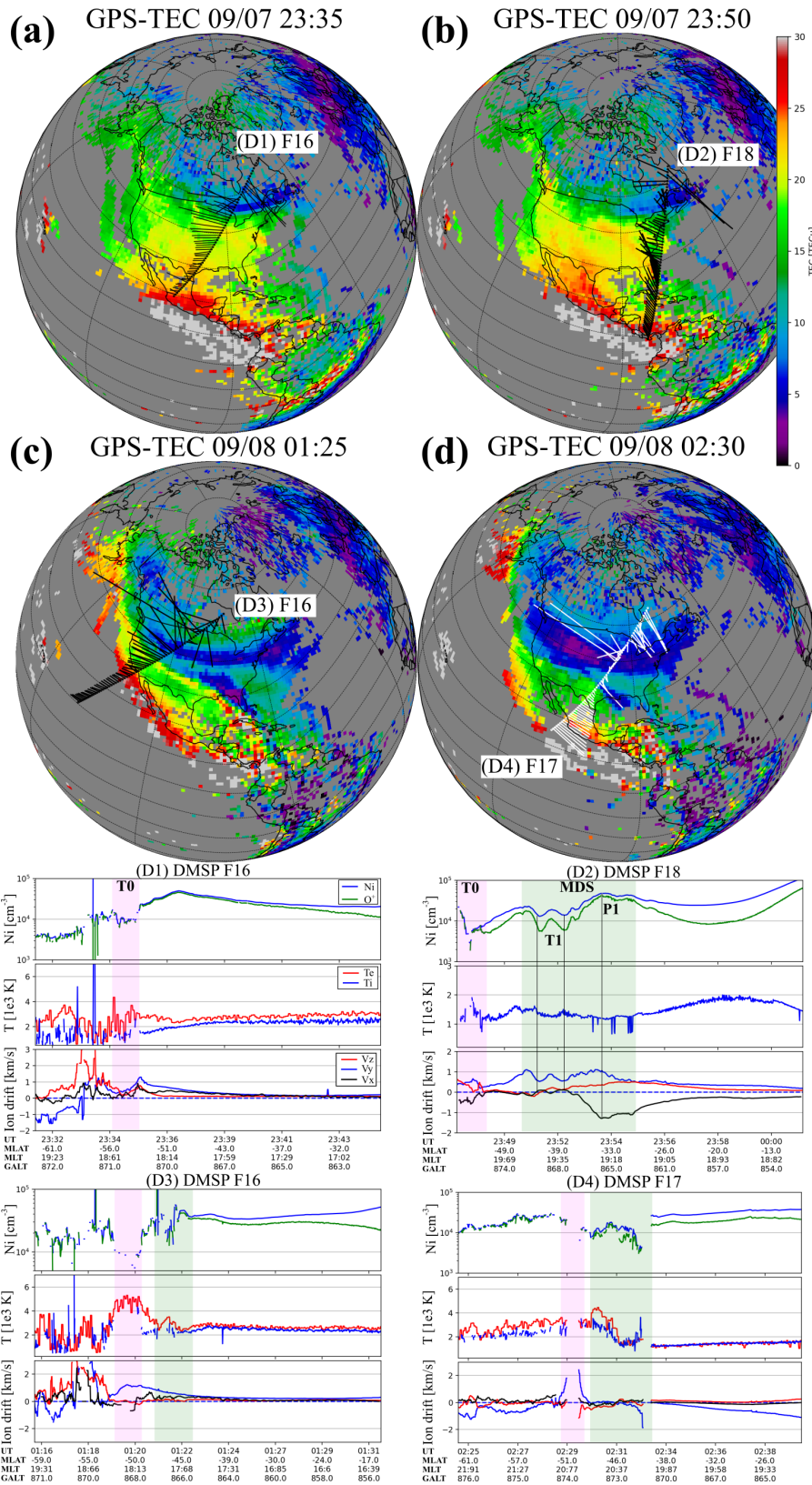


Figure 6. Ionospheric in-situ measurements of ion convection, density and temperatures. (Top panel) DMSP passes with fully resolved horizontal ion flows from selected DMSP passes (F17 vectors lengths are erroneous; see text). Trajectories are mapped to 350 km, matching the background maps of ionospheric TEC. (D1-D4) Panels show DMSP time series measurements; Density plots consist of total ion density (blue) and O^+ abundance (green), ion drift is in the Earth's rotational frame of reference. Magenta-shading denote region of main min-latitude trough T_0 ; green shading mark the MDS area.

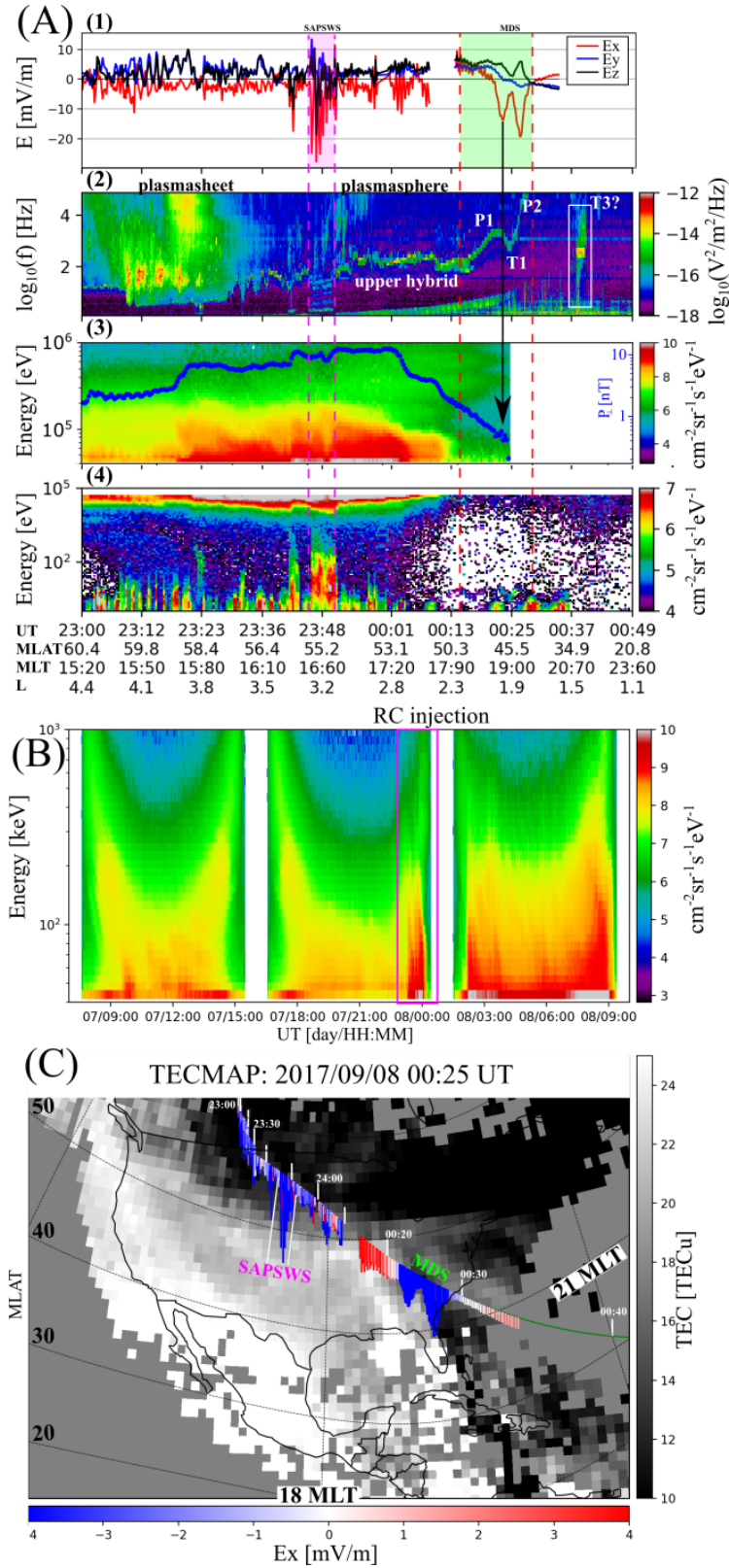


Figure 7. RBSP-A measurements and spacecraft trajectory during the conjugate observations. (A) Measurements of (1) Electric field in solar Magnetic frame of reference; (2) High frequency radio spectra from the HFR instrument, plasma frequency line is a proxy for electron density; (3) RBSPICE energy flux of high energy ions, blue fiducial line is derived perpendicular ion pressure; (4) HOPE energy flux of low energy (<50 keV) ions. (B) Three consecutive orbits of spin averaged ion flux taken by the RBSPICE instrument. The second orbit probed the dusk sector overlapping the panel (A) measurements. Indicative enhancement of <200 keV ion flux is outlined in magenta area. (C) Spacecraft trajectory mapped to northern hemisphere (350 km). Width of the trajectory denotes electric field magnitude, color is modulated by the electric field x-component (proxy for zonal component at given local time). Markers are explained and defined in text. Background is a TEC map at 09/08-00:25 UT.

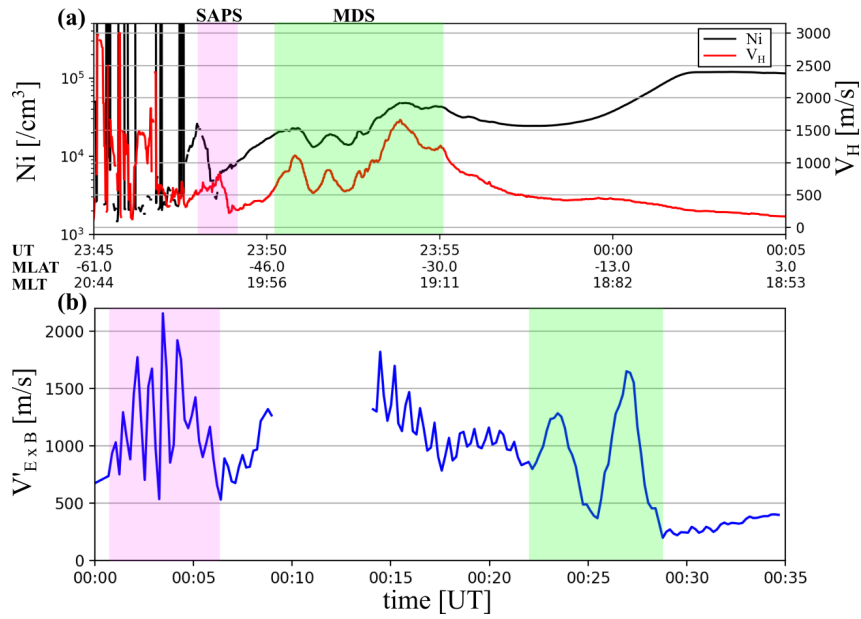


Figure 8. Direct comparison of ionospheric and magnetospheric flow speeds. (a) Measurements of the horizontal ion flow (red) and ion density (black) by the DMSP-F18. (b) Estimated ion flow magnitude at the DMSP height (850 km) by the RBSP-A measurements of electric field. The procedure is defined in text. Magenta and green shading is defined in Figure 6.

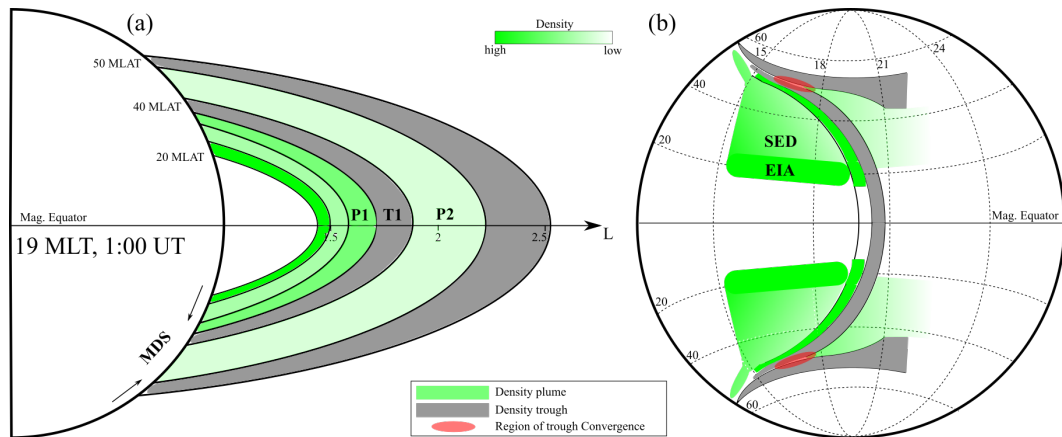


Figure 9. An illustration (not to scale!) of ionosphere-plasmasphere system configuration in geomagnetic cross-sections.